Fe Solubility in the Zn-Rich Corner of the Zn-Al-Fe System for Use in Continuous Galvanizing and Galvannealing

J.R. MCDERMID, M.H. KAYE, and W.T. THOMPSON

The concentration of Al and Fe in molten zinc saturated with delta (~$Fe_2Zn_{10}Al$) or eta (~Fe_2Al_5Zn) intermetallic precipitates has been measured by melt equilibration for temperatures in the range of 450 °C to 480 °C. This information has generated a thermodynamic model for the phase equilibrium in the zinc-rich corner of the Zn-Al-Fe system for the range of compositions and temperatures of commercial interest in continuous galvanizing and galvannealing. The model is constrained by the reported activities of Al in the molten zinc phase and permits small compositional variance of the intermetallic solids. The resultant isothermal phase diagrams are compared with the work of others.

DOI: 10.1007/s11663-007-9028-3

I. INTRODUCTION

THE production of high-quality continuous galvanized (GI) and galvannealed (GA) products requires good bath management practices and, in particular, precise knowledge of the bath dissolved Al concentration.[1–4] Changes in Al concentration, for example, from 0.10 to 0.30 wt pct, have a significant impact on the structure and properties of the resultant coatings by influencing the formation of the so-called "inhibition layer," a 50- to 250-nm-thick layer of the η-$Fe_2Al_5Zn_X$ intermetallic at the substrate/bath interface.[1,5–7] This layer acts as a transient barrier to further reactions between the liquid Zn overlay and the steel. The effectiveness of Al in this role is complicated by the partitioning of Al between the coating and intermetallic compounds that form within the galvanizing bath.[1–6]

At the low bath dissolved Al concentrations commonly employed in the production of GA coatings (*i.e.*, less than 0.14 wt pct at 460 °C), the η-$Fe_2Al_5Zn_X$ layer is thin or discontinuous[1,5–7] and inhibition breakdown (the dissolution/destruction of the η-$Fe_2Al_5Zn_X$ layer) occurs rapidly. This facilitates the transformation of the Zn overlay to the desired sequence of Fe-Zn intermetallics during the subsequent galvannealing operation.[1,8] Conversely, the higher bath dissolved Al concentrations (*i.e.*, greater than 0.15 wt pct) used in producing GI coatings promotes the formation of a continuous, relatively thick η-$Fe_2Al_5Zn_X$ layer in which further reaction of the Fe substrate with the Zn overlay is prevented or inhibited, thereby producing a highly formable, essentially pure Zn metallic coating.[1,5,6] The bath dissolved Al concentration plays a central role in the kinetics of the nucleation and growth process of the inhibition layer,[9–11] as well as in the overall Al concentration in the coating.[7,12] In particular, it is believed that a high Al concentration in the coating has a detrimental effect on the longevity of welding electrodes in spot resistance welding, a commonly employed technology in manufacturing processes involving galvanized or GA steel sheet.[13]

The intermetallic particles found in continuous galvanizing line (CGL) baths are determined by the Al concentration in the molten Zn: ζ-$FeZn_{13}$ at low concentrations; δ-$FeZn_{10}Al_Y$ at intermediate concentrations; and η-$Fe_2Al_5Zn_X$ at higher concentrations,[1–4,14–18] as illustrated in Figure 1.

The origin of these intermetallics in the CGL bath is a direct consequence of the galvanizing bath dissolving Fe until one of the intermetallics phases forms at the bath/substrate interface.[19] Thereafter, the intermetallic species is continuously precipitated from the melt during normal operation of industrial lines.[9,11,16] These particles form a significant portion of the waste product known industrially as "dross." The particles themselves are thought, often erroneously, to be associated with coating defects.[20] In view of the density of the intermetallic phases in relation to liquid Zn, ζ-$FeZn_{13}$ and δ-$FeZn_{10}Al_Y$ are classified as "bottom dross," whereas η-$Fe_2Al_5Zn_X$ is called "top dross."

The intermetallic phases precipitated from the bath have other operational consequences. For example, in CGL baths devoted to the production of GA products, the precipitate is δ-$FeZn_{10}Al_Y$ phase, whereas the precipitate formed during the production of GI products is η-$Fe_2Al_5Zn_X$ phase.[1–4,14–16] The partitioning of Al significantly affects the control methodology used to maintain the target dissolved Al concentration in each of the production regimes.[2–4,21–24] Because many CGLs produce both GA and GI coatings, the transition between these regimes can be problematic due to the differential partitioning of Al.[3,24]

J.R. McDERMID, Associate Professor, is with the Department of Mechanical Engineering, McMaster University, Hamilton, ON, Canada L8S 4L7. Contact e-mail: mcdermid@mcmaster.ca M.H. KAYE, Research Associate, is with the Department of Chemistry and Chemical Engineering, Royal Military College of Canada, Kingston, ON, Canada K7K 7B4. W.T. THOMPSON, Professor, is with the Department of Chemistry and Chemical Engineering, Royal Military College of Canada.

Manuscript submitted January 22, 2006.
Article published online April 27, 2007.

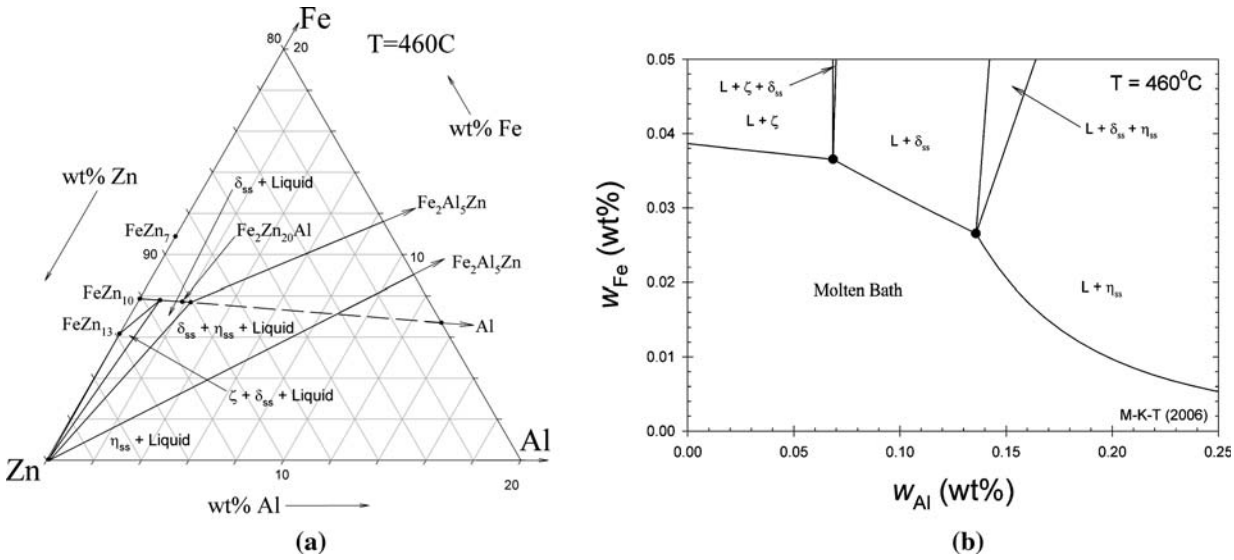

Fig. 1—(*a*) Zn-Al-Fe ternary system, showing the placement of compounds of interest. (*b*) Zn-rich corner of the Zn-Al-Fe ternary system, shifted to Cartesian coordinates.

The determination of the bath dissolved Al and the resident intermetallic species for a given combination of bath Al and Fe requires a detailed knowledge of the Zn-rich corner of the Zn-Al-Fe system. This has proved to be a complex problem and has been the subject of significant research effort,[16–18,25–39] and has also been recently reviewed by Rajhavan.[40] The main difficulty lies in the complex nature of the equilibria between the various intermetallic phases in the Zn-rich corner and the Zn-Al-Fe liquid. This continues to be a subject of discussion.[14–18,25–39]

Tang and co-workers advocate a Zn-rich liquid phase that, in order of increasing bath Al concentration, coexists with ζ-$FeZn_{13}$, δ-$FeZn_7$, and either η-$Fe_2Al_5Zn_X$[29,31] or Γ'-Fe_5Zn_{21} and η-$Fe_2Al_5Zn_X$[30] or, most recently, T (a ternary solution phase) and η-$Fe_2Al_5Zn_X$.[34] It is noteworthy that the ζ-$FeZn_{13}$, δ-$FeZn_{10}$, Γ_2-$Fe_8Zn_{86}Al_6$, and η-$Fe_2Al_5Zn_X$ configuration was later advocated by Perrot *et al.*[28] for equilibration times of 1000 hours, where the composition of their Γ_2 phase is very close to that of the T phase of Tang and Su.[34] All versions of the diagram have a similar basic shape, but there is significant disagreement in Fe solubility, however, in the region of lower Al concentrations.[18,26,27,29–31,34,37–39]

Unfortunately, only limited experimental solubility data and related thermodynamic data have been published. Giorgi *et al.*[32] have published a thermodynamic model for the Zn-rich corner of the Zn-Al-Fe system using the solubility limits of Tang[31] and the ternary Al activity data of Yamaguchi.[14] A similar study, recently made by Costa e Silva *et al.*,[33] was not as successful, with difficulties being encountered with the δ and Γ' phases arising from the lack of curvature of the Fe solubility[30] in the region of the δ and Γ' phases.

The objectives of the present work were to perform independent experimental studies to determine the solubility of Fe as a function of Al concentration in the molten alloy phase and to use these data as a basis for improved thermodynamic modeling of the Zn-rich corner of the Zn-Al-Fe phase diagram for application in continuous galvanizing and galvannealing. The activity measurements of Yamaguchi[14] were incorporated into the analysis.

II. EXPERIMENTAL PROCEDURE

Solubility experiments were carried out in the industrially relevant bath temperature range of 450 °C to 480 °C with temperature increments of 5 °C between 450 °C and 470 °C. The Al concentration was varied between 0.09 and 0.25 wt pct at increments of 0.01 wt pct, thereby encompassing the range of commercial interest.[1–4] The Fe concentration was increased to precipitate intermetallic phases, which were later identified by metallographic analysis. The melt composition was subsequently varied with the addition of Al, with occasional Fe additions being made to ensure that the bath Fe concentration continued to exceed the solubility limit. Additional experiments were performed to fill in data gaps as the basic shape of the solubility curves became evident and to obtain finer resolution on the transition from the δ-$FeZn_{10}Al_Y$ phase region to the η-$Fe_2Al_5Zn_X$ phase region. All experiments were run in duplicate and, in selected cases, triplicate.

Experiments were carried out in the Noranda Galvanizing Simulator, a 2.5 m^3 atmosphere controlled glove box in which all of the required experimental apparatus resided, employing the resident 20-kg bath. The bath crucible used was composed of high-purity graphite, heated in a resistance furnace with the temperature controlled by a type K thermocouple to ± 2 °C. The crucible was cleaned prior to each experiment to prevent cross-contamination. The temperature/time profile for each run was recorded during the equilibration period to

monitor possible thermal excursions. Oxidation of the melt was prevented by using dry N_2. Special high-grade (SHG, ASTM B6[41]) Zn was used for the bulk bath and 99.99 pct purity Al and Fe were added to the melt as chopped wire. The bath was allowed to equilibrate for 30 minutes after complete dissolution of the alloy additions. The melt was mildly stirred during this time, and the bath was skimmed prior to sampling.

Quartz pin tube samples (3.5-mm diameter) were taken from the center of the crucible to prevent excessive contamination of the samples by the increased presence of dross particles near the top and bottom of the crucible. These were water quenched immediately following sampling to prevent precipitation of intermetallic particles during sample cooling. Multiple samples were taken from each bath for chemical and metallographic analysis. Chemical analysis results were averaged to obtain a single data point at that composition. Samples for chemical analysis were dissolved in a 10 pct HCl solution and analyzed in triplicate with ICP using the technique of matrix matched standards for the analysis calibration. This method is considered to be accurate to ± 5 pct of the reported concentration for both solute elements.

Pin tube samples took two forms: nonfiltered and filtered samples. Filtered samples were obtained by passing the molten bath metal through a 50-μm pore size rigid-bond ZrO_2 filter material using a vacuum pump.[42] This method effectively removed the vast majority of intermetallic particles of a size greater than 1 μm to yield a sample that could be analyzed directly to obtain the dissolved Al and Fe concentrations. To ensure that the filtration process was satisfactory, all filtered samples were examined using optical metallography for the presence of large intermetallic particles. The nonfiltered samples were used for three purposes: (1) to link the total Al and Fe sample analysis to a particular filtered sample analysis; (2) to ensure that the bulk bath coexisted with intermetallic phases; and (3) to establish the composition of these intermetallic phases. The latter was performed using quantitative X-ray microanalysis (EDX) in a scanning electron microscope (SEM, acceleration voltage 20 kV) on metallographic cross sections of the nonfiltered samples using the atomic weight-absorption-fluorescence spectrum correction technique. This technique is accurate to ± 0.5 wt pct. The wt pct Fe/wt pct Al ratio determined for each filtered and nonfiltered sample pair was correlated to the composition of the coexisting intermetallic phase, thereby establishing the ends of a tie-line. Only particles larger than 5 μm were selected for the EDX analysis to minimize excessive X-ray interaction with the surrounding matrix.

The phase fields and their boundaries were approximately established through intermetallic species identification. Empirical equations for the solubility curves as a function of temperature and bath composition were established based on the chemical analysis of the filtered samples. These equations were used to guide the subsequent thermodynamic modeling efforts.

III. SOLUBILITY EXPERIMENT RESULTS

All the experimental solubility data are shown in Tables I through III. The vast majority of particles

Table I. Filtered Sample Chemical Analysis at 450 °C and 455 °C and the Intermetallic(s) Present in the Corresponding Nonfiltered (NF) Sample; All Chemical Analyses are Accurate to ±5 Pct

	Filtered Samples				Filtered Samples		
T (°C)	Al (Wt Pct)	Fe (Wt Pct)	NF Sample Intermetallic	T (°C)	Al (Wt Pct)	Fe (Wt Pct)	NF Sample Intermetallic
450	0.0957	0.0238	δ_{SS}	455	0.0951	0.0281	δ_{SS}
450	0.0976	0.0242	δ_{SS}	455	0.1001	0.0239	δ_{SS}
450	0.1143	0.0245	δ_{SS}	455	0.1173	0.0270	δ_{SS}
450	0.1162	0.0194	δ_{SS}	455	0.1195	0.0240	δ_{SS}
450	0.1234	0.0227	δ_{SS}	455	0.1233	0.0227	δ_{SS}
450	0.1295	0.0198	$\delta_{SS} + \eta_{SS}$	455	0.1258	0.0245	δ_{SS}
450	0.1315	0.0220	$\delta_{SS} + \eta_{SS}$	455	0.1308	0.0200	$\delta_{SS} + \eta_{SS}$
450	0.1346	0.0178	η_{SS}	455	0.1321	0.0248	$\delta_{SS} + \eta_{SS}$
450	0.1371	0.0196	η_{SS}	455	0.1326	0.0264	$\delta_{SS} + \eta_{SS}$
450	0.1448	0.0166	η_{SS}	455	0.1422	0.0224	η_{SS}
450	0.1465	0.0183	η_{SS}	455	0.1446	0.0192	η_{SS}
450	0.1507	0.0133	η_{SS}	455	0.1469	0.0201	η_{SS}
450	0.1529	0.0161	η_{SS}	455	0.1507	0.0171	η_{SS}
450	0.1534	0.0146	η_{SS}	455	0.1542	0.0157	η_{SS}
450	0.1678	0.0125	η_{SS}	455	0.1545	0.0162	η_{SS}
450	0.1779	0.0108	η_{SS}	455	0.1655	0.0155	η_{SS}
450	0.1836	0.0102	η_{SS}	455	0.1741	0.0121	η_{SS}
450	0.2022	0.0086	η_{SS}	455	0.1810	0.0125	η_{SS}
450	0.2052	0.0086	η_{SS}	455	0.1963	0.0090	η_{SS}
450	0.2155	0.0068	η_{SS}	455	0.1996	0.0102	η_{SS}
450	0.2228	0.0072	η_{SS}	455	0.2055	0.0086	η_{SS}
450	0.2440	0.0067	η_{SS}	455	0.2176	0.0083	η_{SS}
				455	0.3576	0.0029	η_{SS}

Table II. Filtered Sample Chemical Analysis at 460 °C and 465 °C and the Intermetallic(s) Present in the Corresponding Nonfiltered Sample (All Chemical Analyses are Accurate to ± 5 Pct); Compositions (1) through (3) at 460 °C are Samples for Which Micrographs of the Nonfiltered Sample Intermetallic Particles are Shown in Figure 2

T (°C)	Filtered Samples		NF Sample Intermetallic	T (°C)	Filtered Samples		NF Sample Intermetallic
460	0.0932	0.0271	δ_{SS}	465	0.0966	0.0303	δ_{SS}
460	0.0947	0.0282	δ_{SS}	465	0.1038	0.0291	δ_{SS}
460	0.1155	0.0277	δ_{SS}	465	0.1155	0.0301	δ_{SS}
460	0.1161	0.0269	δ_{SS}	465	0.1200	0.0296	δ_{SS}
460	0.1240	0.0273	δ_{SS}	465	0.1234	0.0315	δ_{SS}
(1)460	**0.1249**	**0.0316**	δ_{SS}	465	0.1278	0.0291	δ_{SS}
460	0.1276	0.0265	δ_{SS}	465	0.1290	0.0310	δ_{SS}
460	0.1332	0.0263	$\delta_{SS} + \eta_{SS}$	465	0.1353	0.0275	$\delta_{SS} + \eta_{SS}$
460	0.1335	0.0255	$\delta_{SS} + \eta_{SS}$	465	0.1375	0.0286	$\delta_{SS} + \eta_{SS}$
(2)460	**0.1341**	**0.0278**	$\delta_{SS} + \eta_{SS}$	465	0.1388	0.0241	η_{SS}
460	0.1355	0.0220	$\delta_{SS} + \eta_{SS}$	465	0.1465	0.0271	η_{SS}
460	0.1373	0.0223	η_{SS}	465	0.1470	0.0224	η_{SS}
460	0.1450	0.0210	η_{SS}	465	0.1526	0.0253	η_{SS}
460	0.1531	0.0220	η_{SS}	465	0.1541	0.0197	η_{SS}
460	0.1545	0.0194	η_{SS}	465	0.1543	0.0185	η_{SS}
460	0.1574	0.0178	η_{SS}	465	0.1669	0.0166	η_{SS}
460	0.1680	0.0142	η_{SS}	465	0.1673	0.0200	η_{SS}
460	0.1693	0.0154	η_{SS}	465	0.1887	0.0156	η_{SS}
(3)460	**0.1808**	**0.0125**	η_{SS}	465	0.1918	0.0137	η_{SS}
460	0.1909	0.0116	η_{SS}	465	0.2015	0.0103	η_{SS}
460	0.1963	0.0089	η_{SS}	465	0.2078	0.0119	η_{SS}
460	0.1990	0.0092	η_{SS}	465	0.2217	0.0111	η_{SS}

found in the experimental samples were either δ-$FeZn_{10}Al_Y$ (δ_{SS}) or η-$Fe_2Al_5Zn_X$ (η_{SS}), as few examples of the ζ-$FeZn_{13}$ intermetallic were found and no such compositions are reported here.

The compositional values of the intermetallic species from the literature are presented in Table IV, and the values for the chemical analyses of the intermetallic particles in the present work are shown in Table V. A comparison shows good agreement. The stoichiometry of the δ-$FeZn_{10}Al_Y$ phase in the present study conforms to a Fe:Zn molar ratio of approximately 1:10 and the Fe:Al ratio of the η-$Fe_2Al_5Zn_X$ particle to approximately 2:5.

The data indicated in Table II correspond to the SEM micrographs in Figure 2. Point 1 is an example of the δ-$FeZn_{10}Al_Y$ intermetallic. Point 3 is an example of η-$Fe_2Al_5Zn_X$. The range of compositions of these intermetallics is listed in Table V.

Point 2 in Table II shows both the δ_{SS} and η_{SS} phases. The chemical analysis of filtered samples from this three-phase region showed an invariant dissolved Al bath concentration in the liquid phase (within experimental error) consistent with the phase rule, and these samples were used to establish the bounding tie-lines of the three-phase field ($\delta_{SS} + \eta_{SS} + L$).

Very few ζ-$FeZn_{13}$ particles were encountered in the SEM/EDX analysis of the nonfiltered samples. Thus, insufficient experimental data were available to determine the limits of the ζ-$FeZn_{13}$ phase field and the precise placement of the ζ-$FeZn_{13}$, δ-$FeZn_{10}Al_Y$, and liquid-phase triple point. Determination of the limits of the ζ-$FeZn_{13}$ phase field was, therefore, established through the thermodynamic data used in the modeling stage of the study.

IV. THERMODYNAMIC MODELING

An overview of the Zn-Al-Fe ternary system, showing the position of the compounds of interest, was shown in Figure 1(a) and enlarged in the area of commercial interest in Figure 1(b). In this region, δ_{SS} and η_{SS} are to be found in equilibrium with the Zn-rich liquid. The ζ phase may coexist with liquid up to 530 °C.

A. *Liquid Zn-Rich Phase*

The estimation of properties in the ternary alloy to obtain the interaction parameters was accomplished with the aid of the Kohler interpolation,[43] as illustrated in Figure 3. The suitability of this interpolation scheme and rationale for its selection are discussed elsewhere.[44–46]

This approach requires a model for the excess Gibbs energies, G^E_{i-j}, for each of the bounding binary subsystems. With reference to Figure 3, the integral excess Gibbs energy, G^E, at any point in the ternary mixture can be estimated with the equation:[44]

$$G^E = (1 - X_{Fe})^2 G^E_{Zn-Al} + (1 - X_{Al})^2 G^E_{Fe-Zn} + (1 - X_{Zn})^2 G^E_{Fe-Al} \quad [1]$$

where the integral excess Gibbs energies in the binary subsystems Zn-Al,[47] Fe-Zn,[48] and Fe-Al[49] are given by points a, b, and c, respectively, and X_i is the mole fraction of component i in the solution. The partial excess Gibbs energies, $\overline{G}^E_i$, can then be obtained by differentiation with respect to the mole fraction of

Table III. Filtered Sample Chemical Analysis at 470 and 480°C and the Intermetallic(s) Present in the Corresponding Nonfiltered Sample; All Chemical Analyses are Accurate to ±5 Pct

T (°C)	Filtered Samples		NF Sample Intermetallic	T (°C)	Filtered Samples		NF Sample Intermetallic
470	0.1048	0.0375	δ_{SS}	480	0.0953	0.0481	δ_{SS}
470	0.1125	0.0344	δ_{SS}	480	0.0959	0.0527	δ_{SS}
470	0.1153	0.0338	δ_{SS}	480	0.1111	0.0420	δ_{SS}
470	0.1162	0.0370	δ_{SS}	480	0.1147	0.0431	δ_{SS}
470	0.1216	0.0306	δ_{SS}	480	0.1209	0.0415	δ_{SS}
470	0.1237	0.0379	δ_{SS}	480	0.1248	0.0409	δ_{SS}
470	0.1261	0.0340	δ_{SS}	480	0.1284	0.0376	δ_{SS}
470	0.1308	0.0346	δ_{SS}	480	0.1301	0.0484	δ_{SS}
470	0.1312	0.0334	δ_{SS}	480	0.1321	0.0375	δ_{SS}
470	0.1330	0.0357	δ_{SS}	480	0.1324	0.0392	δ_{SS}
470	0.1366	0.0334	$\delta_{SS} + \eta_{SS}$	480	0.1359	0.0393	$\delta_{SS} + \eta_{SS}$
470	0.1379	0.0368	δ_{SS}	480	0.1388	0.0405	$\delta_{SS} + \eta_{SS}$
470	0.1385	0.0331	$\delta_{SS} + \eta_{SS}$	480	0.1404	0.0367	$\delta_{SS} + \eta_{SS}$
470	0.1392	0.0293	$\delta_{SS} + \eta_{SS}$	480	0.1422	0.0384	η_{SS}
470	0.1397	0.0373	$\delta_{SS} + \eta_{SS}$	480	0.1434	0.0371	η_{SS}
470	0.1413	0.0307	$\delta_{SS} + \eta_{SS}$	480	0.1508	0.0351	η_{SS}
470	0.1425	0.0317	$\delta_{SS} + \eta_{SS}$	480	0.1605	0.0287	η_{SS}
470	0.1471	0.0274	η_{SS}	480	0.1618	0.0281	η_{SS}
470	0.1486	0.0300	η_{SS}	480	0.1761	0.0245	η_{SS}
470	0.1561	0.0260	η_{SS}	480	0.1880	0.0293	η_{SS}
470	0.1596	0.0206	η_{SS}	480	0.1916	0.0182	η_{SS}
470	0.1664	0.0239	η_{SS}	480	0.1953	0.0217	η_{SS}
470	0.1664	0.0208	η_{SS}	480	0.3375	0.0064	η_{SS}
470	0.1696	0.0202	η_{SS}	480	0.4255	0.0038	η_{SS}
470	0.1751	0.0174	η_{SS}				
470	0.1788	0.0192	η_{SS}				
470	0.1818	0.0176	η_{SS}				
470	0.1830	0.0195	η_{SS}				
470	0.1834	0.0161	η_{SS}				
470	0.1849	0.0150	η_{SS}				
470	0.1867	0.0187	η_{SS}				
470	0.1974	0.0156	η_{SS}				
470	0.2020	0.0143	η_{SS}				
470	0.2048	0.0132	η_{SS}				
470	0.2224	0.0118	η_{SS}				

Table IV. Chemical Composition of CGL Intermetallics Taken from the Literature[15–18]

Phase	Wt Pct Al	Wt Pct Fe	Wt Pct Zn	Fe/Al
ζ-$FeZn_{13}$	0.7 to 1.0	5.8 to 6.1	93.2	N/A
δ-$FeZn_{10}Al_Y$ (bottom dross particle)	1.5 to 3.5	2.2 to 9.5	87 to 93.0	1.55 to 5.3
η-$Fe_2Al_5Zn_X$ (top dross particle)	37 to 46	31 to 37	18 to 25	0.7 to 0.9

Table V. Composition of Bath Intermetallics in the Present Study

Phase	Wt Pct Al	Wt Pct Fe	Wt Pct Zn	At. Pct Al	At. Pct Fe	At. Pct Zn
δ-$FeZn_{10}Al_Y$	2.16 ± 1.79	7.62 ± 0.63	90.58 ± 2.02	4.97 ± 3.98	8.58 ± 0.63	87.29 ± 3.87
η-$Fe_2Al_5Zn_X$	43.98 ± 1.30	39.08 ± 0.62	16.67 ± 1.80	63.18 ± 1.13	26.97 ± 0.25	9.85 ± 1.20

the component. Because the partial excess Gibbs energy of component i is related to the activity coefficient, γ_i, by

$$\bar{G}_i^E = RT \ln \gamma_i \quad [2]$$

the activity of a particular element at a given composition can be generated from Eqs. [1] and [2]. This makes it possible to express explicitly the activity coefficient of Al or Fe in the form often used for dilute metallic solutions.[44,50]

$$\ln \gamma_{Al} = \ln \gamma_{Al}^{\circ} + \ln \gamma_{Zn} + \varepsilon_{Al-Al} X_{Al} + \varepsilon_{Fe-Al} X_{Fe} \quad [3]$$

$$\ln \gamma_{Fe} = \ln \gamma_{Fe}^{\circ} + \ln \gamma_{Zn} + \varepsilon_{Fe-Fe} X_{Fe} + \varepsilon_{Al-Fe} X_{Al} \quad [4]$$

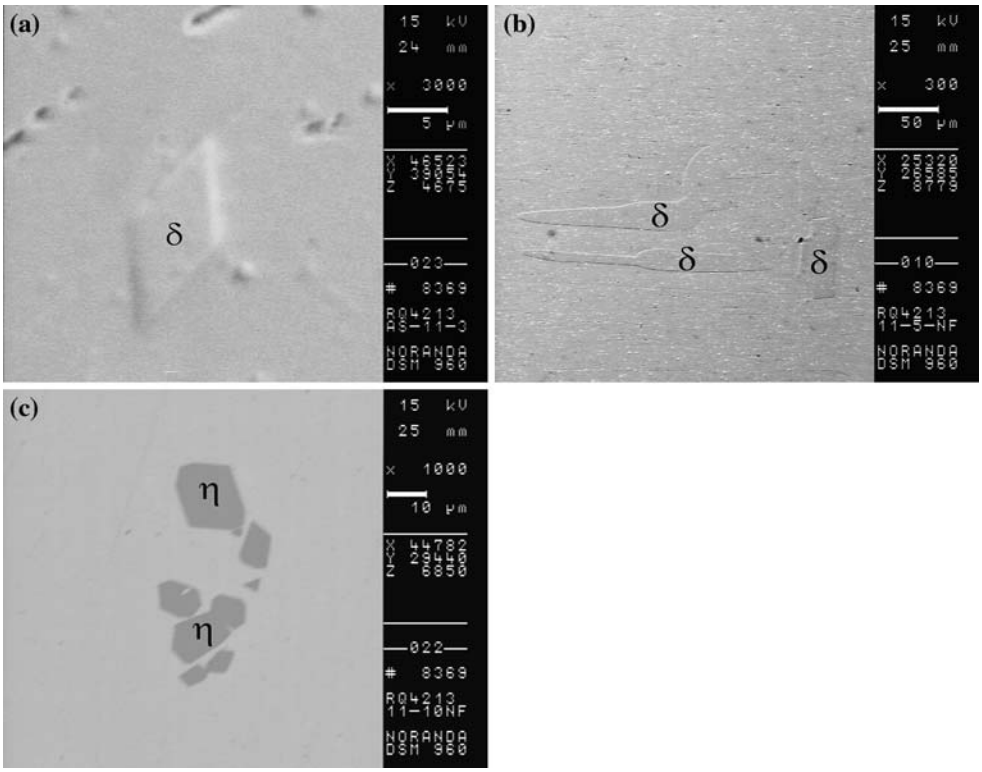

Fig. 2—SEM micrographs of typical bath intermetallic particles at experimental points 1 through 3 in Table II. The intermetallic species were identified by EDX, the general compositions of which can be seen in Table V.

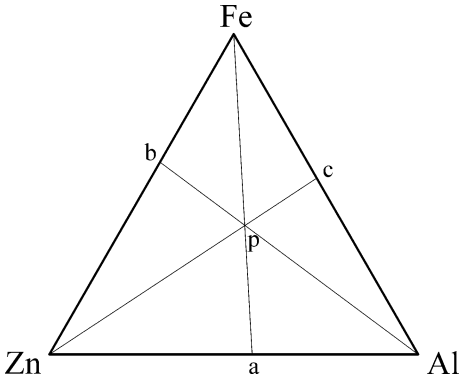

Fig. 3—Ternary diagram illustrating the Kohler interpolation[43] (Eq. [1]) for determining the excess Gibbs energy at point *p*, from the properties of the binary subsystems at *a*, *b*, and *c*.

where

$$\ln \gamma_{Zn} = -\frac{1}{2}\left[\varepsilon_{Al-Al}X_{Al}^2 + \varepsilon_{Fe-Fe}X_{Fe}^2 + 2\varepsilon_{Fe-Al}X_{Fe}X_{Al}\right] \quad [5]$$

γ_i° is the Henrian activity coefficient of species *i*, and ε_{i-j} are the interaction parameters. When the solution is very dilute, as in the present situation, ln γ_{Zn} is nearly zero and this term may be ignored. The matter of establishing the interaction parameters ε_{i-j} will now be discussed.

1. *Zn-Al subsystem*

An endeavour was made to bring the features of the binary Al-Zn phase diagram into alignment with the thermodynamic properties of Murray.[47] The excess Gibbs energy was reported as

$$G_{Liq}^E = X_{Al}X_{Zn}(-11,479 + 24.12T) + X_{Al}X_{Zn}^2(4880) \quad \text{J/mol} \quad [6]$$

These parameters are not sufficient to describe the activities of the components in the ternary system as measured by Yamaguchi.[14] In view of the scatter of the experimental thermodynamic data[47] in support of Eq. [6], a small third term was added, as shown in Eq. [7]:

$$G_{Liq}^E = X_{Al}X_{Zn}(-11,479+24.12T) + X_{Al}X_{Zn}^2(4880) + X_{Al}X_{Zn}^3(35,317-52.50T) \quad \text{J/mol} \quad [7]$$

The effect of this addition is shown in Figure 4. The effect is to shift the maximum toward the Al side of the figure, but the Al-rich region remains virtually unchanged.

As a further point of comparison, the partial Gibbs energy of Al in dilute Zn solution, when projected to 1000 K, based on Eq. [7], is now in good agreement with

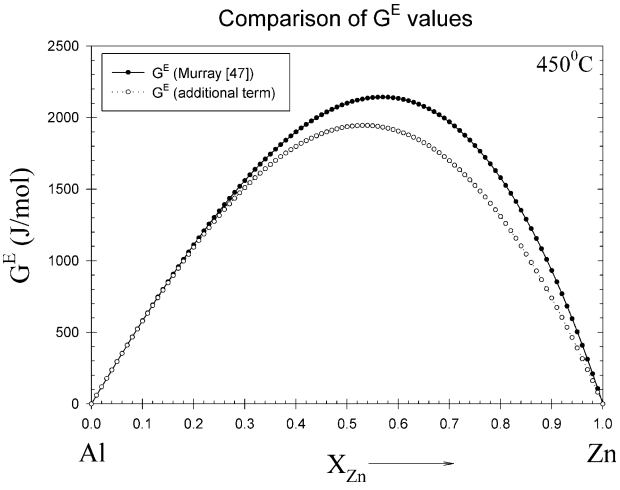

Fig. 4—Comparison of the excess Gibbs energy at 450 °C for the liquid phase of the Al-Zn system.

the updated treatment of the Al-Zn binary phase diagram by an Mey.[51]

2. *Zn-Fe subsystem*

For the excess contribution to the liquid from the Zn-Fe system, the equilibrium between the liquid and the ζ phase was considered. The Gibbs energy of formation for the ζ phase from the elements in their standard states, developed from Su *et al.*,[52] is consistent with Reumont *et al.*[53] and Burton and Perrot.[48] The resulting excess property for the liquid, rich in Zn, is given by the equation, where X_{Zn} is greater than 0.99:

$$G^E_{\text{Liq}} = X_{\text{Fe}}X_{\text{Zn}}(-51,244 + 71.77T) \quad \text{J/mol} \qquad [8]$$

3. *Al-Fe subsystem*

Finally, for the excess contribution to the liquid phase from the Al-Fe subsystem, a regular solution model[44] was employed:

$$G^E_{Liq} = X_{Al}X_{Fe}(300,000) \quad \text{J/mol} \qquad [9]$$

The numerical parameter, which influences the interpolation in Eq. [1], was adjusted to respect the measured activity of aluminum[14] in the zinc-rich ternary melt. Equation [9] is used only to generate the required thermodynamic properties of the liquid in the Zn-rich corner of Figure 3 and cannot be used to extrapolate thermodynamic properties outside of this region of the diagram. Its use is confined to Eq. [1]. Table VI summarizes all the excess Gibbs energy parameters for the liquid-phase model.

From the data in Table VI and applying the dilute solution formalism discussed previously,[44] the limiting activity coefficient of Fe in molten Zn (with respect to pure solid α-Fe) is

Table VI. Excess Gibbs Energy Parameters for the Binary Subsystems of the Liquid Phase

Coefficients	Parameters (J/mol)
$X_{\text{Al}}X_{\text{Zn}}$	–11,479 + 24.12 T
$X_{\text{Al}}X^2_{\text{Zn}}$	+4880
$X_{\text{Al}}X^3_{\text{Zn}}$	+35,317 – 52.50 T
$X_{\text{Fe}}X_{\text{Zn}}$	–51,244 + 71.77 T
$X_{\text{Al}}X_{\text{Fe}}$	+300,000

$$\ln \gamma^o_{\text{Fe}} = \frac{-1628.4}{T} + 3.008 \qquad [10]$$

where T is the absolute temperature in Kelvin. Similarly, the limiting activity of Al in molten Zn (with respect to pure solid Al) is

$$\ln \gamma^o_{\text{Al}} = \frac{2053.8}{T} - 2.074 \qquad [11]$$

Finally, from Eqs. [3] and [4], the interaction effects between Al and Fe are

$$\varepsilon_{\text{Al-Al}} = \frac{-10,828.8}{T} + 13.854 \qquad [12]$$

$$\varepsilon_{\text{Fe-Fe}} = \frac{5266.6}{T} - 7.377 \qquad [13]$$

$$\varepsilon_{\text{Fe-Al}} = \varepsilon_{\text{Al-Fe}} = \frac{16,122}{T} - 1.395 \qquad [14]$$

B. *ζ solid ($FeZn_{13}$)*

No significant solubility data were collected in the present investigation for the ζ phase. Although some authors[18,31] have indicated that there is a small variable Al solubility (less than 2 at pct), this has not been incorporated into the present work because it will not significantly effect the placement of the solubility curve. The properties of stoichiometric ζ were derived using the liquid-phase treatment discussed previously to respect the peritectic decomposition at 530 °C on the Fe-Zn phase diagram, the measured properties of Su *et al.*,[52] and the recent work of Nakano *et al.*[54] Thus, for ζ, $\Delta H^\circ_{298} = -45,710.0$ J/mol and $S^\circ_{298} = 563.84$ J/K/mol. The more recent measurements[52] are in accord with the solubility data of Kubaschewski.[55] Table VII compares the Zn mole fraction in the ζ saturated liquid of Su *et al.*[52] with the present treatment.

C. *δ-Solid Solution (δ_{SS}) (approximately $Fe_2Zn_{20}Al$)*

The δ_{SS} was formulated taking the components to be $FeZn_{10}$ and Al. The properties were adjusted to describe

Table VII. Zn Mole Fraction in the ζ-Saturated Zn-Fe Liquid: Comparison of Su *et al.*[52] with the Present Treatment (M-K-T 2006)

Temperature	Su *et al.*[52] X_{Zn}	(M-K-T 2006) X_{Zn}
420 °C	0.9999	0.99984
450 °C	0.99965	0.99965
460 °C	0.99955	0.99955
530 °C	0.997	0.99774

the measured solubilities near the δ_{SS} + η_{SS} + L triple point. For stoichiometric δ-$FeZn_{10}$, $\Delta H^{\circ}_{298} = -53,132.5$ J/mol and $S^{\circ}_{298} = 425$ J/K/mol. These properties, in conjunction with those previously discussed for $FeZn_{13}$, provide for a peritectic in the Fe-Zn binary system at 530 °C. For Al dissolved in the δ_{SS} phase, the activity coefficient was adjusted to represent the solubility measurements previously discussed.

$$\ln \gamma_{Al} = \frac{2433.93}{T} - 63.744 \qquad [15]$$

The product of γ_{Al}, given by Eq. [15], and the mole fraction of Al in an $FeZn_{10}$-Al δ_{SS} phase give the activity of Al with respect to pure solid Al.

With this treatment for the δ-solid solution, the composition for this phase ranges from $Fe_2Zn_{20}Al_{1.21}$ to $Fe_2Zn_{20}Al_{0.32}$. This encompasses the nominal value of $Fe_2Zn_{20}Al$ cited previously and by other authors[15–18] but provides for a variable Fe to Al proportion, as indicated by the chemical analyses in the present study and the data in Reference 31.

D. *η-Solid Solution (η_{SS}) (Approximately Fe_2Al_5Zn)*

Fe_2Al_5 and Zn were selected as the components for the η-solid solution. The properties of each were adjusted to describe the measured solubilities near the δ_{SS} + η_{SS} + L triple point, its exact placement, and the reduced Fe solubility at higher Al concentrations. The available data for the concentration of Zn in the η-solid solution[15–18] and the results of the present investigation shown in Table V further constrain the selection of the parameters. The properties for hypothetical η-Fe_2Al_5 are $\Delta H^{\circ}_{298} = -150,580.1$ J/mol and $S^{\circ}_{298} = 249.78$ J/K/mol. These are similar to the properties suggested by Kattner for pure Fe_2Al_5.[49] To represent the solubility of Zn dissolved in the η_{SS} phase, the activity coefficient was

$$\ln \gamma_{Zn} = \frac{481.09}{T} \qquad [16]$$

In this case, it was unnecessary to incorporate a second (constant) term in Eq. [16].

In the present context, the composition of η_{SS} is approximately Fe_2Al_5Zn at any temperature. This agrees with Ajersch *et al.*,[15] Toussaint *et al.*,[16] Chen *et al.*,[17] Perrot *et al.*,[18] and the chemical analyses in this investigation.

V. DISCUSSION

Computed ternary diagrams at 450 °C, 455 °C, 460 °C, 465 °C, 470 °C, and 480 °C are shown in Figures 5 through 10, respectively, in relation to the measured solubility data reported in Tables I through III. The experimental data show good agreement with the thermodynamic treatment within the 5 pct uncertainty limit associated with the ICP technique. The placement of the phase boundaries is similar to previous treatments by the present authors, particularly the η_{SS} + L boundary.[37–39] The most significant adjustments in the present treatment are as follows: the

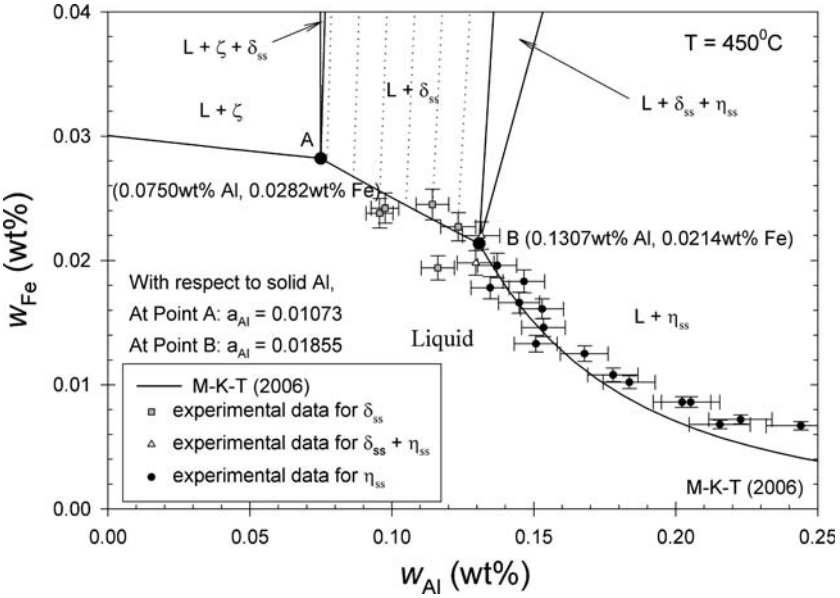

Fig. 5—Comparison of the Zn-Al-Fe ternary in the Zn-rich corner at 450 °C with the solubility measurements from Table I.

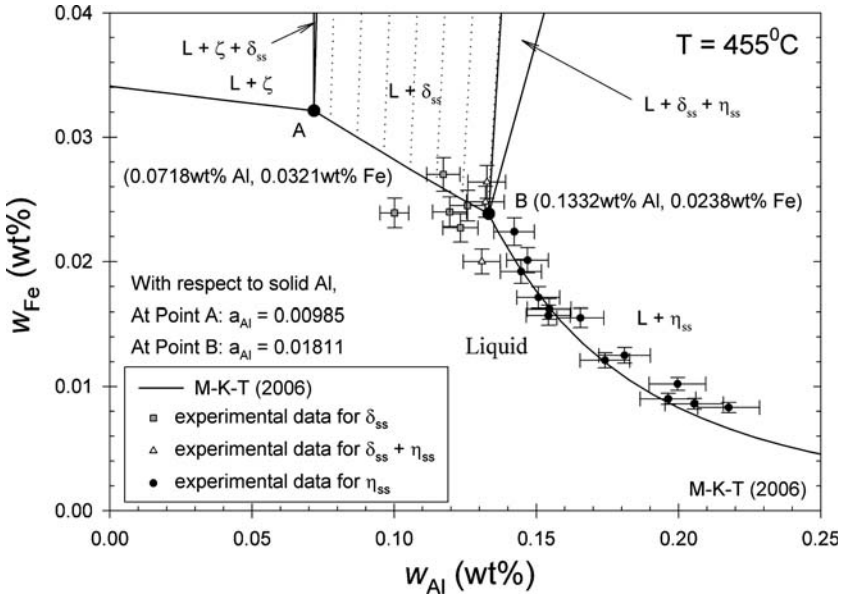

Fig. 6—Comparison of the Zn-Al-Fe ternary in the Zn-rich corner at 455 °C with the solubility measurements from Table I.

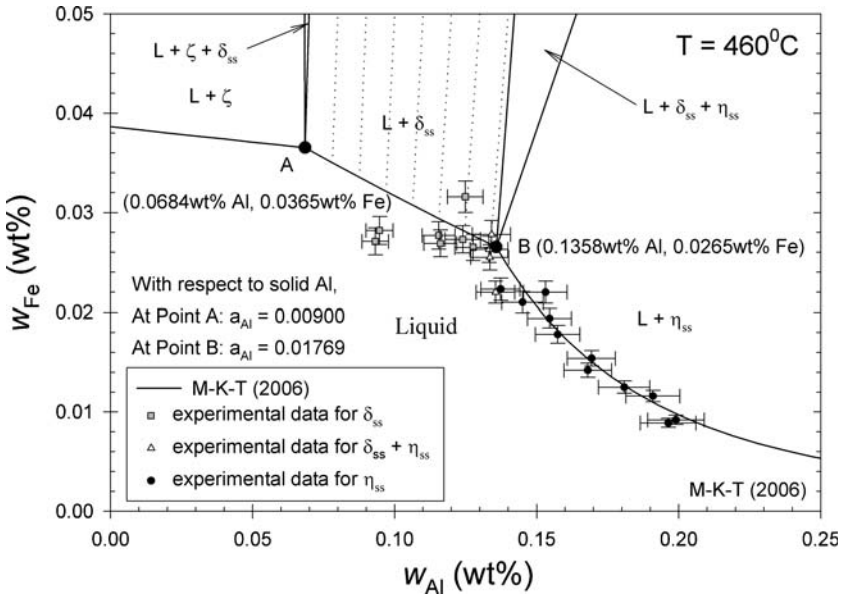

Fig. 7—Comparison of the Zn-Al-Fe ternary in the Zn-rich corner at 460 °C with the solubility measurements from Table II.

solubility of the δ_{SS} phase, the provision for variable Al and Zn concentration in the δ_{SS} and η_{SS} phases, and the incorporation of the activity data of Yamaguchi.[14]

As shown in Table VIII, the computed activity of Al (with respect to solid Al) at the δ_{SS} + η_{SS} + L triple point is in good agreement with the electrochemical measurements of Yamaguchi.[14] Increasing the fidelity of the aluminum activity representation was a goal of this treatment.

Details of the activity of Fe (referred to α-Fe) and Al (referred to solid Al) as they vary with composition in the liquid phase are shown in Figures 11 through 14, respectively, at 450 °C, 460 °C, 470 °C, and 480 °C. Details of the calculated triple points (*A* and *B*) over the interval 420 °C to 480 °C are provided in Table IX.

Figure 15 shows the 460 °C phase diagram from the present treatment in relation to the most recent version of Tang.[31] The two sets of solubility curves are generally in agreement for the placement of point *B* and the solubility curve in the η_{SS} + L region, differing mainly in the placement of point *A* and the curvature of the solubility of δ_{SS} and ζ.

The solubility of η, represented as a solubility product by Tang,[31] is

$$\ln\,[\mathrm{Fe}]^2[\mathrm{Al}]^5 = 28.1 - \frac{33,066}{T} \qquad [17]$$

which can be compared to the present treatment approximately represented in the same form:

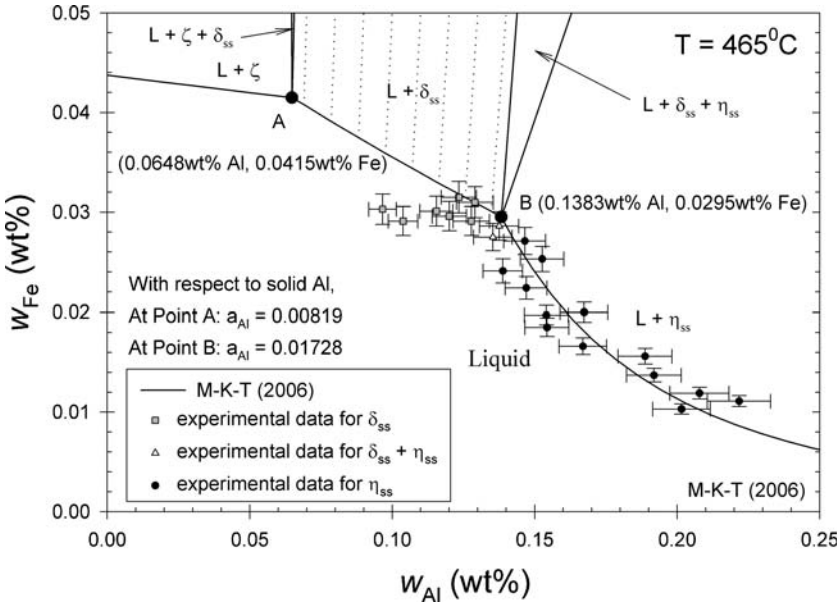

Fig. 8—Comparison of the Zn-Al-Fe ternary in the Zn-rich corner at 465 °C with the solubility measurements from Table II.

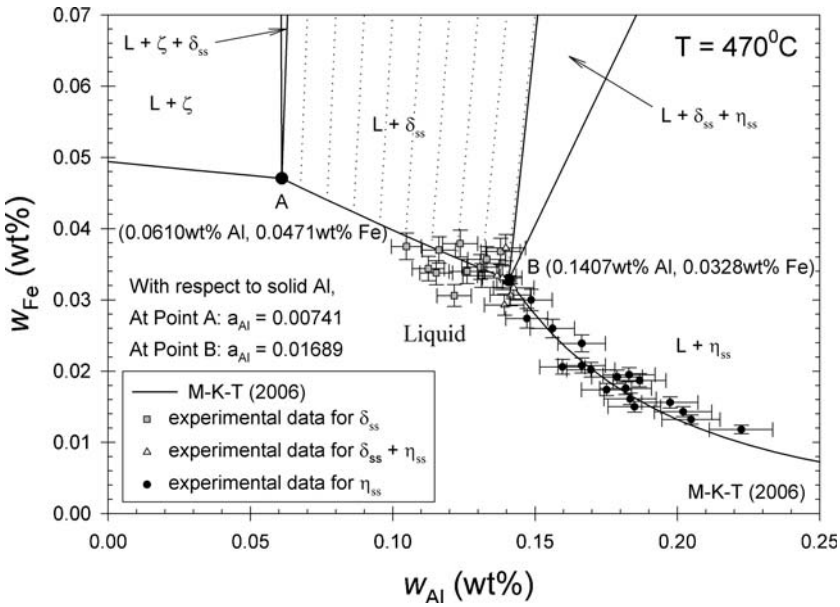

Fig. 9—Comparison of the Zn-Al-Fe ternary in the Zn-rich corner at 470 °C with the solubility measurements from Table III.

$$\ln [\mathrm{Fe}]^2[\mathrm{Al}]^5 \simeq 23.711 \pm 7.596 - \frac{29,993 \pm 5593}{T} \quad (r^2 = 0.82) \quad [18]$$

In these equations, [X] represents the concentration of the element in the liquid (wt pct), and T is the temperature in Kelvin. The r^2 value associated with Eq. [18] shows that the equation adequately represents the experimental data. Within the 95 pct confidence limit for the coefficients in Eq. [18], there is agreement with Eq. [17].[31]

The differences in the δ_{SS} solubility arise principally from the variable composition used for δ_{SS} in the present analysis (Table IX). The approximate δ_{SS} solubility product derived from the experimental data in the present work is given by

$$\ln [\mathrm{Fe}]^2[\mathrm{Al}] \simeq 24.449 \pm 5.932 - \frac{24760 \pm 4380}{T} \quad (r^2 = 0.89) \quad [19]$$

The r^2 value of Eq. [19] adequately represents the experimental data and thermodynamic treatment of the $\delta_{SS} + L$ solubility curve.

The variation of the Al concentration in the δ_{SS} is consistent with the experimental observations in the

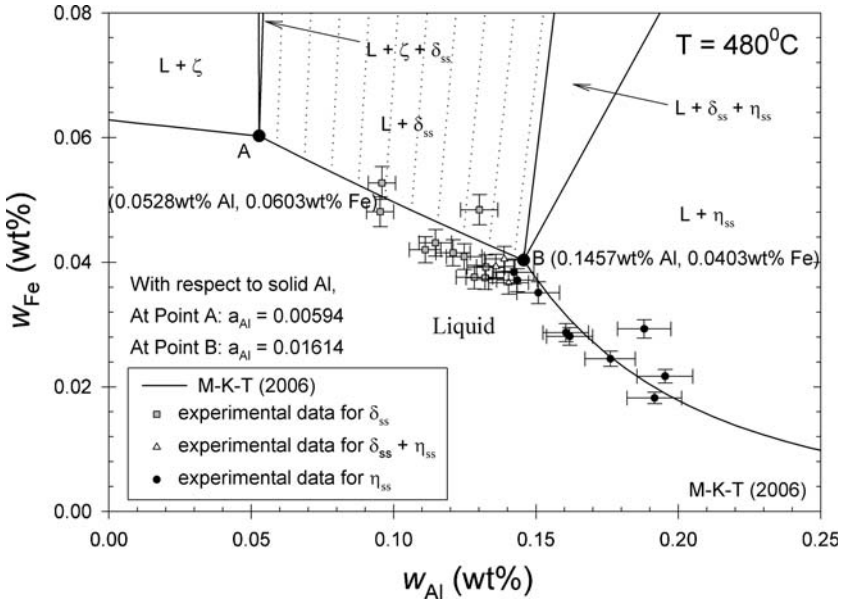

Fig. 10—Comparison of the Zn-Al-Fe ternary in the Zn-rich corner at 480 °C with the solubility measurements from Table III.

Table VIII. Comparison of Al Activity (with Respect to Fcc Al) at the δ_{SS} + η_{SS} + L Triple Point B

Temperature (°C)	Calculated Composition (B)		(M-K-T 2006)	Yamaguchi[14]
	Wt Pct Al	Wt Pct Fe	a_{Al}	a_{Al}
420	0.1154	0.0108	0.0215	0.0218
430	0.1205	0.0136	0.0205	0.0206
440	0.1256	0.0171	0.0195	0.0196
450	0.1307	0.0214	0.0185	0.0186
455	0.1332	0.0238	0.0181	0.0181
460	0.1358	0.0265	0.0177	0.0177
465	0.1383	0.0295	0.0173	0.0173
470	0.1407	0.0328	0.0169	0.0169
480	0.1457	0.0403	0.0161	0.0161

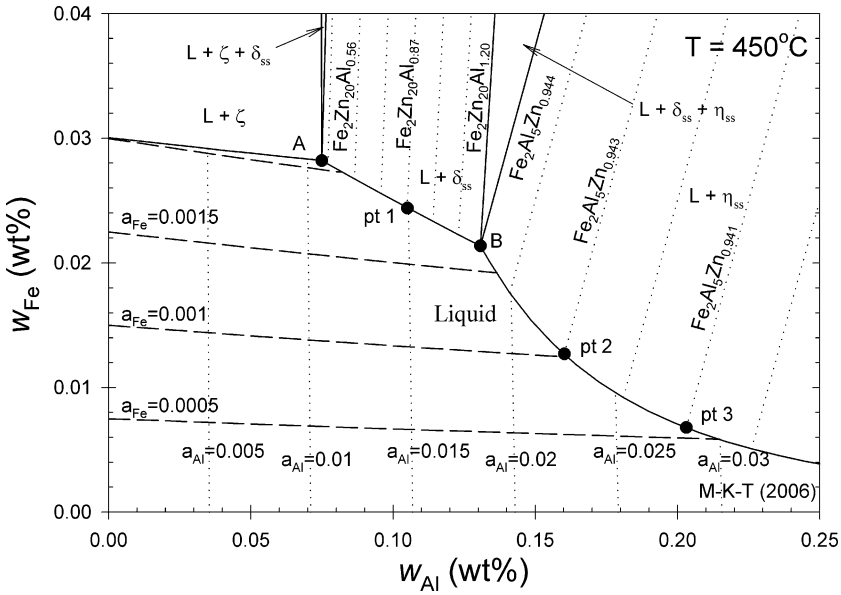

Fig. 11—Activity of Al and Fe at 450 °C. Compositional details at the other temperatures appear in Table IX .

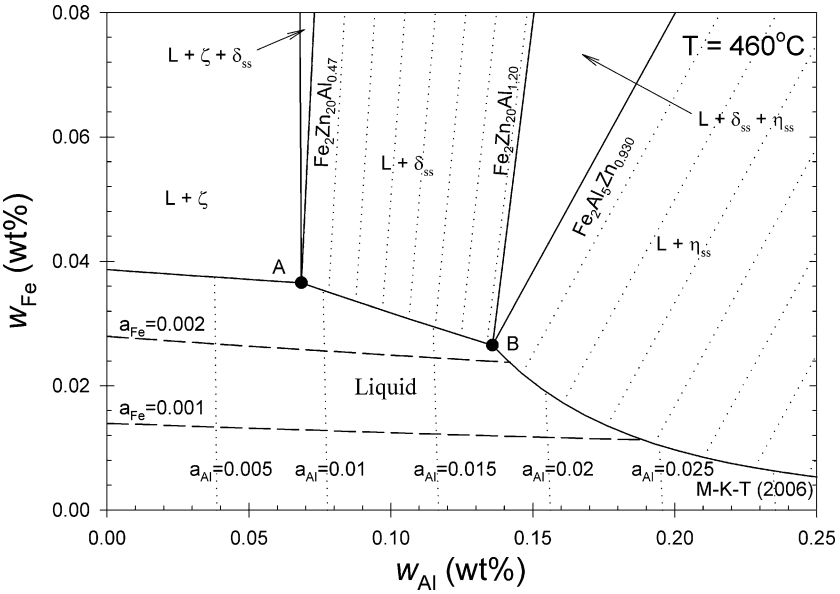

Fig. 12—Activity of Al and Fe at 460 °C.

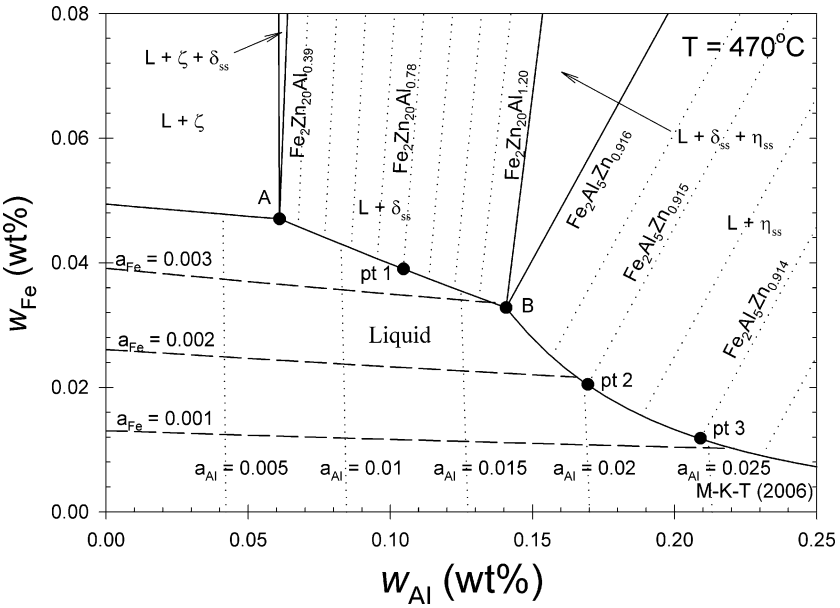

Fig. 13—Activity of Al and Fe at 470 °C.

present study (Table V) and is also consistent with those of Ajersch *et al.*[15] and Perrot *et al.*[18] The range of Al concentration in the δ_{SS} phase is wider than that of Tang,[31] and this phase exists over a wider variation in dissolved aluminum concentration. The curvature of the δ_{SS} solubility is a consequence of the variation in Al concentration in this phase.

A. *Application to Bath Management*

One of the most persistent commercial concerns is the continuous formation of intermetallic particles in the galvanizing bath, which in part leads to the formation of dross. Temperature changes in the CGL bath can exacerbate this problem.[2,3]

A series of diagrams, enlarged about point B, are presented in Figure 16. Points 1 through 3 represent the total Al and Fe concentration of the alloy, held constant for all temperatures. At 470 °C, each point represents a saturated, but intermetallic precipitate-free bath. The effect of cooling from 470 °C to 450 °C (typical of CGL thermal fluctuation about the operating temperature of 460 °C) on the relative proportions of each of the phases is indicated. As the composition of the bath at point 1 cools, only δ_{SS} precipitates. For point 2, only η_{SS} precipitates. Between these two points, representing the

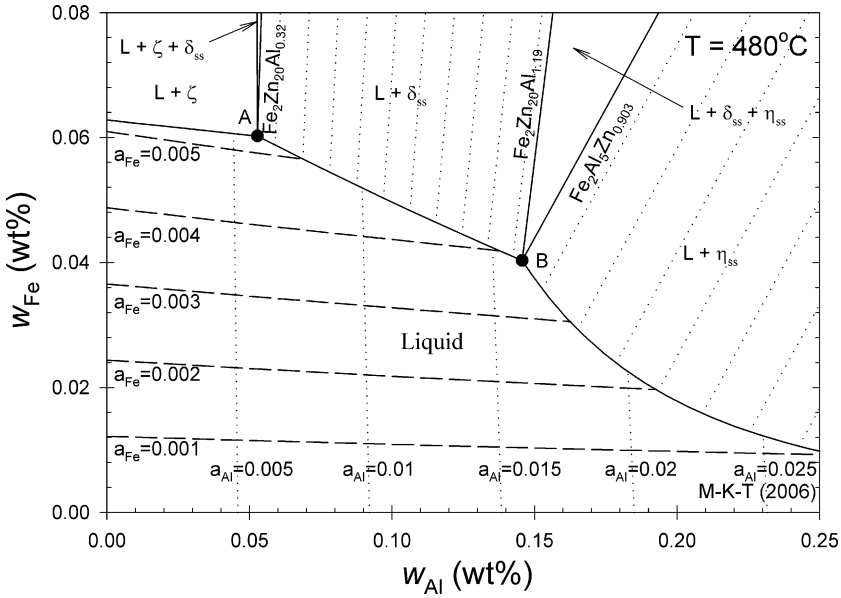

Fig. 14—Activity of Al and Fe at 480 °C.

Table IX. Liquid Compositions at the Triple Points A and B and Related Information

T (°C)	Point	Al (Wt Pct)	Fe (Wt Pct)	Stoichiometry Delta solid	Point	Al (Wt Pct)	Fe (Wt Pct)	Stoichiometry Eta Solid
420	A	0.0900	0.0125	$Fe_2Zn_{20}Al_{0.84}$				
420	B	0.1154	0.0108	$Fe_2Zn_{20}Al_{1.21}$	B	0.1154	0.0108	$Fe_2Al_5Zn_{0.991}$
430	A	0.0858	0.0165	$Fe_2Zn_{20}Al_{0.74}$				
430	B	0.1205	0.0136	$Fe_2Zn_{20}Al_{1.21}$	B	0.1205	0.0136	$Fe_2Al_5Zn_{0.975}$
440	A	0.0808	0.0216	$Fe_2Zn_{20}Al_{0.64}$				
440	B	0.1256	0.0171	$Fe_2Zn_{20}Al_{1.21}$	B	0.1256	0.0171	$Fe_2Al_5Zn_{0.959}$
450	A	0.0750	0.0282	$Fe_2Zn_{20}Al_{056}$	B	0.1307	0.0214	$Fe_2Al_5Zn_{0.944}$
450	1	0.1050	0.0244	$Fe_2Zn_{20}Al_{0.87}$	2	0.1602	0.0127	$Fe_2Al_5Zn_{0.943}$
450	B	0.1307	0.0214	$Fe_2Zn_{20}Al_{1.20}$	3	0.2031	0.0068	$Fe_2Al_5Zn_{0.941}$
455	A	0.0718	0.0321	$Fe_2Zn_{20}Al_{0.51}$				
455	B	0.1332	0.0238	$Fe_2Zn_{20}Al_{1.20}$	B	0.1332	0.0238	$Fe_2Al_5Zn_{0.937}$
460	A	0.0684	0.0365	$Fe_2Zn_{20}Al_{0.47}$				
460	B	0.1358	0.0265	$Fe_2Zn_{20}Al_{1.20}$	B	0.1358	0.0265	$Fe_2Al_5Zn_{0.930}$
465	A	0.0648	0.0415	$Fe_2Zn_{20}Al_{0.43}$				
465	B	0.1383	0.0295	$Fe_2Zn_{20}Al_{1.20}$	B	0.1383	0.0295	$Fe_2Al_5Zn_{0.923}$
470	A	0.0610	0.0471	$Fe_2Zn_{20}Al_{0.39}$	B	0.1407	0.0328	$Fe_2Al_5Zn_{0.916}$
470	1	0.1046	0.0390	$Fe_2Zn_{20}Al_{0.78}$	2	0.1695	0.0205	$Fe_2Al_5Zn_{0.915}$
470	B	0.1407	0.0328	$Fe_2Zn_{20}Al_{1.20}$	3	0.2091	0.0118	$Fe_2Al_5Zn_{0.914}$
480	A	0.0528	0.0603	$Fe_2Zn_{20}Al_{0.32}$				
480	B	0.1457	0.0403	$Fe_2Zn_{20}Al_{1.19}$	B	0.1457	0.0403	$Fe_2Al_5Zn_{0.903}$

extremes of Al concentrations for GA and GI production, point 3 represents a transitional composition. Initially, δ_{SS} precipitates, but at lower temperatures, η_{SS} coprecipitates as well.

Considering the total mass of a typical galvanizing bath, the mass percentages of intermetallics evident in Figure 16 represent a significant mass of dross, and, in the cases where η_{SS} is involved, also represent a significant loss of Al *via* partitioning to the top dross. This results in the ineffective use of Al bath additions and complicates the control of the bath composition. It is, therefore, evident that a numerical treatment of the phase equilibria is of value, particularly during excursions in temperature combined with shifts in production mode from GA to GI when Al is added.[56]

VI. CONCLUSIONS

Solubility experiments and thermodynamic modeling were performed in order to delineate the Zn-rich corner of the Zn-Al-Fe phase diagram for use in continuous galvanizing and galvannealing. A thermodynamic model,

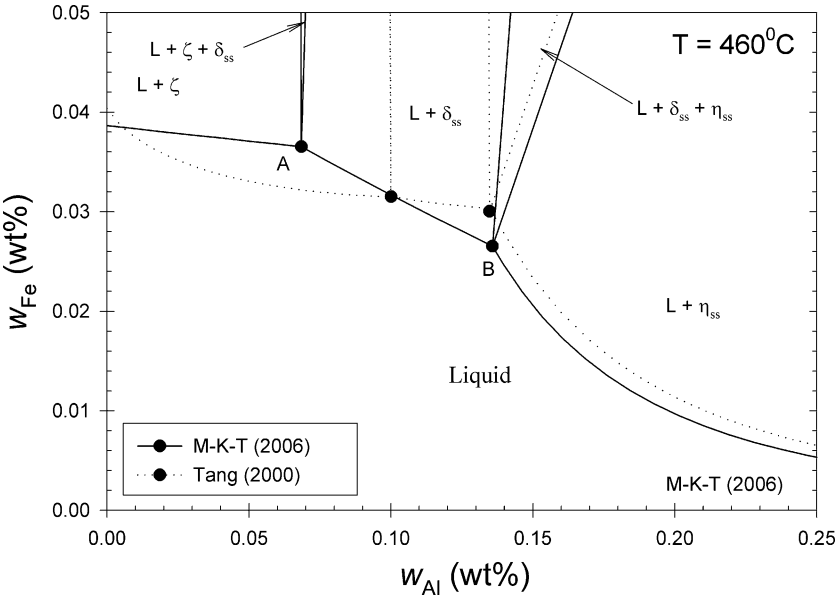

Fig. 15—Comparison of the present model (M-K-T (2006)) to that of Tang[31] at 460 °C.

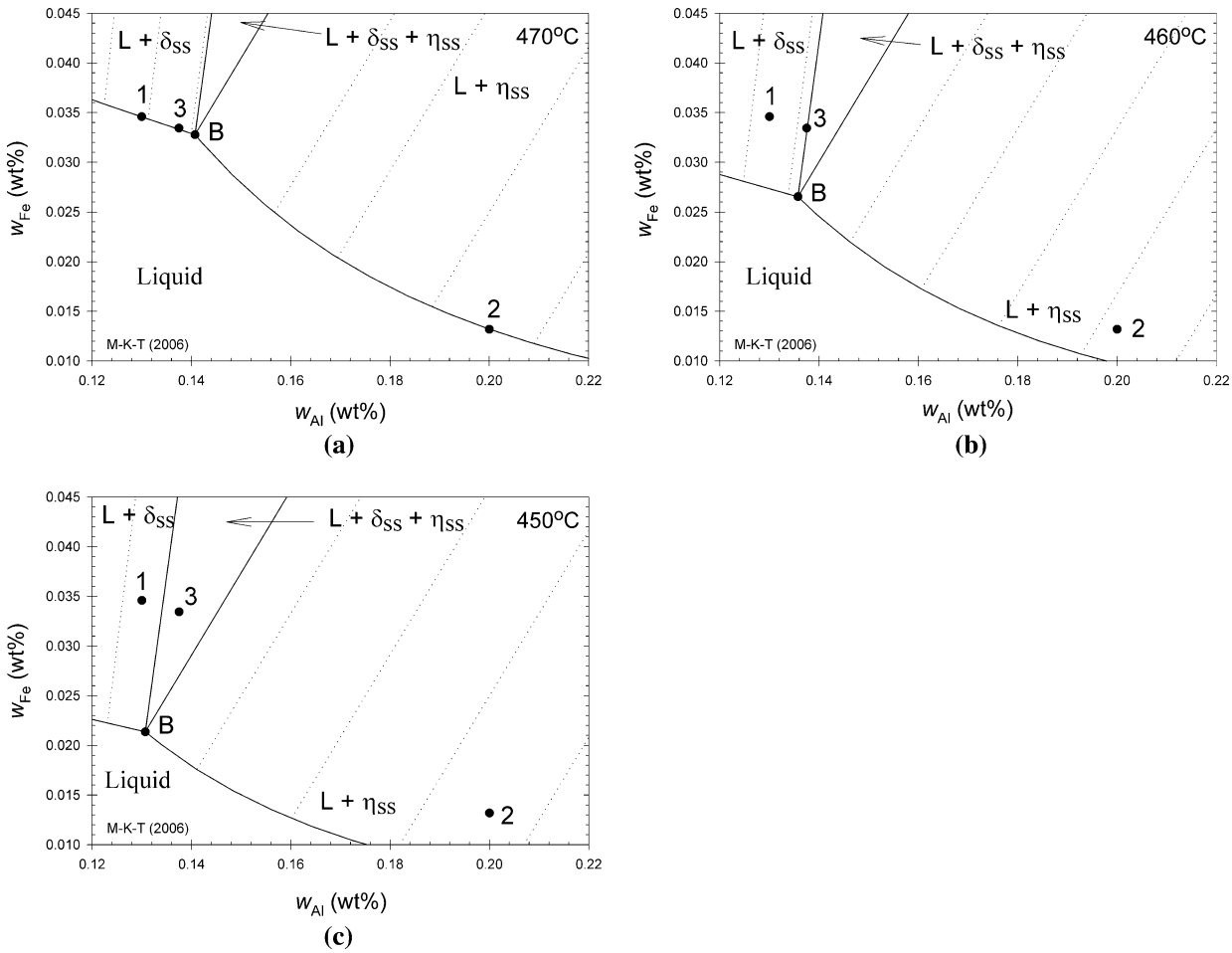

Fig. 16—Detail of precipitation in the vicinity of point B.

based on the Kohler interpolation of the binary systems, was developed to generate solubility curves and triple points consistent not only with the experimental data but also the reported Al activity.[14] Variable concentration of Al and Zn in the δ-$FeZn_{10}Al_Y$ (δ_{SS}) and η-$Fe_2Al_5Zn_X$ (η_{SS}) intermetallics was incorporated into the model. The resultant phase diagram is similar to that of Tang[31] in the high Al (η_{SS} + L region), but differs in the positioning of the phase boundaries in the lower Al (δ_{SS} + L and ζ + L phase regions). The discussion draws attention to the need for a numerical treatment of the phase equilibrium in assisting bath control of continuous galvanizing lines.

ACKNOWLEDGMENTS

The experiments were performed while J.R. McDermid was a Senior Scientist at the former Noranda Inc.–Technology Centre. The authors thank Falconbridge Inc. for their permission to publish this work. The authors also thank Mr. B. Henshaw for performing the solubility experiments and the staff in the Analytical Chemistry Laboratory for performing the chemical analyses and the metallography. J.R. McDermid and W.T. Thompson acknowledge the Natural Sciences and Engineering Research Council of Canada (NSERC) for financial support of this work.

TABLE OF SYMBOLS

G^E	integral excess Gibbs energy
G_i^E	integral excess Gibbs energy of phase *i*
G_{i-j}^E	integral excess Gibbs energy in binary system *i-j*
$\bar{G}_i^E$	partial excess Gibbs energy of component *i*
ΔH_{298}°	standard enthalpy of formation at 298 K
S_{298}°	standard entropy at 298 K
L	liquid
R	universal gas constant
X_i	mole fraction of component *i*
δ_{SS}	delta solid solution
ε_{A-B}	interaction coefficient of component *B* on *A*
η_{SS}	eta solid solution
γ_i	activity coefficient of component *i*
γ_i°	Henrian activity coefficient of component *i* (*i.e.*, infinite dilution)
ζ	$FeZn_{13}$ phase

REFERENCES

1. A.R. Marder: *Prog. Mater. Sci.*, 2000, vol. 45, pp. 191–271.
2. N.-Y. Tang, M. Dubois, and F.E. Goodwin: *4th Int. Conf. on Zinc and Zinc Alloy Coated Steel Sheet: Galvatech '98 Conf. Proc.*, Chiba, Japan, 1998, Iron and Steel Institute of Japan, 1998, pp. 76–83.
3. J.R. McDermid, E. Baril, and F.E. Goodwin: *6th Int. Conf. on Zinc and Zinc Alloy Coated Steel Sheet: Galvatech '04 Conf. Proc.*, Chicago, IL, 2004, Association for Iron and Steel Technology, 2004, pp. 855–69.
4. N.-Y. Tang: *Metall. Mater. Trans. B*, 1999, vol. 30B, pp. 144–48.
5. E. Baril and G. L.'Espérance: *Metall. Mater. Trans. A*, 1999, vol. 30A, pp. 681–95.
6. N.-Y. Tang, and G.R. Adams: in *The Physical Metallurgy of Zinc Coated Steel*, A.R. Marder, ed., TMS, Warrendale, PA, 1993, pp. 41–54.
7. V. Furdanowicz and C.D. Shastry: *Metall. Mater. Trans. A*, 1999, vol. 30A (12), pp. 3031–44.
8. S. Dionne, G. Botton, M. Charest, and F.E. Goodwin: *Proc. Int. Symp. on Materials in the Automotive Industry*, Montreal, 2001, E. Essadiqi, F.E. Goodwin, and M. Elboujaini, eds., TMS-CIM, 2001, pp. 351–66.
9. N.-Y. Tang: *Metall. Mater. Trans. A*, 1995, vol. 26A, pp. 1699–704.
10. P. Toussaint, L. Segers, R. Winand, and M. Dubois: *ISIJ Int.*, 1998, vol. 38 (9), pp. 985–90.
11. M.-L. Giorgi, J.-B. Guillot, and R. Nicolle: *6th Int. Conf. on Zinc and Zinc Alloy Coated Steel Sheet: Galvatech '04 Conf. Proc.*, Chicago, IL, 2004, Association for Iron and Steel Technology, 2004, pp. 703–72.
12. M. Dubois: *6th Int. Conf. on Zinc and Zinc Alloy Coated Steel Sheet: Galvatech '04 Conf. Proc.*, Chicago, IL, 2004, Association for Iron and Steel Technology, 2004, pp. 1079–88.
13. H. Matsuda, Y. Matsuda, and M. Kabasawa: *Weld. Int.*, 1996, vol. 10 (8), pp. 605–13.
14. S. Yamaguchi: *4th Int. Conf. on Zinc and Zinc Alloy Coated Steel Sheet: Galvatech '98 Conf. Proc.*, Chiba, Japan, 1998, Iron and Steel Institute of Japan, 1998, pp. 84–89.
15. F. Ajersch, L. Trépanier, and F.E. Goodwin: *44th Mechanical Working and Steel Processing Conf. Proc.*, Orlando, FL, 2002, Iron and Steel Society, 2002, vol. XL, pp. 771–80.
16. P. Toussaint, L. Segers, R. Winand, and M. Dubois: *Iron Steelmaking*, 1995, vol. 22 (6), pp. 498–501.
17. Z.W. Chen, R.M. Sharpe, and J.T. Gregory: *Mater. Sci. Technol.*, 1990, vol. 6, pp. 1173–76.
18. P. Perrot, J.-C. Tissier, and J.-Y. Dauphin: *Z. Metallkd.*, 1992, vol. 83 (11), pp. 786–90.
19. J. Nakano, G.R. Purdy, and D.V. Malakhov: *XXXI CALPHAD Meeting*, Stockholm, May 2002.
20. N.-Y. Tang and F.E. Goodwin: *5th Int. Conf. on Zinc and Zinc Alloy Coated Steel Sheet: Galvatech '01 Conf. Proc.*, Brussels, Belgium, 2001, pp. 49–55.
21. N.-Y. Tang: *Proc. 92nd Galvanizer's Association Meeting*, Toronto, 2000, Galvanizer's Association, 2000.
22. T. Le and M. Gagné: *5th Int. Conf. on Zinc and Zinc Alloy Coated Steel Sheet: Galvatech '01 Conf. Proc.*, Brussels, Belgium, 2001, Verlag-Stahleisen, Düsseldorf, Germany, 2001, pp. 533–39.
23. Y.H. Liu and N.-Y. Tang: *Proc. 94th Galvanizer's Association Meeting*, Dearborn, MI, 2002, Galvanizer's Association, 2002.
24. J.R. McDermid and C.E. Dewey: *Proc. 92nd Galvanizer's Association Meeting*, Toronto, 2000, Galvanizer's Association, 2000.
25. M. Urednicek and J.S. Kirkaldy: *Z. Metallkd.*, 1973, vol. 64 (6), pp. 419–27.
26. S. Bélisle, V. Lezon, and M. Gagné: *J. Phase Equil.*, 1991, vol. 12 (3), pp. 259–65.
27. M. Dauzat, F. Stouvenot, and T. Moreau: *2nd Int. Conf. on Zinc and Zinc Alloy Coated Steel Sheet: Galvatech '92 Conf. Proc.*, Amsterdam, Netherlands, Stahleisen, Düsseldorf, Germany, 1992, pp. 449–54.
28. P. Perrot, G. Reumont, J.-C. Tissier, and J. Foct: *3rd Int. Conf. on Zinc and Zinc Alloy Coated Steel Sheet: Galvatech '95 Conf. Proc.*, Chicago, IL, 1995, Iron and Steel Society, Warrendale, PA, 1995, pp. 763–67.
29. N.-Y. Tang: *Mater. Sci. Technol.*, 1995, vol. 11, pp. 870–73.
30. N.-Y. Tang: *J. Phase Equil.*, 1996, vol. 17 (5), pp. 396–98.
31. N.-Y. Tang: *J. Phase Equil.*, 2000, vol. 21 (1), pp. 70–77.
32. M.-L. Giorgi, J.-B. Guillot, and R. Nicolle: *Calphad*, 2001, vol. 25 (3), pp. 461–74.
33. A. Costa e Silva, R.R. Avillez, and K. Marques: *Z. Metallkd.*, 1999, vol. 90 (1), pp. 38–43.
34. N.-Y. Tang and X. Su: *Metall. Mater. Trans. A*, 2002, vol. 33A, pp. 1559–61.

35. S. Yamaguchi, N. Fukatsu, H. Kimura, K. Kawamura, Y. Iguchi, and T.O. Hashi: *3rd Int. Conf. on Zinc and Zinc Alloy Coated Steel Sheet: Galvatech '95 Conf. Proc.*, Chicago, IL, 1995, Iron and Steel Society, Warrendale, PA, 1995, pp. 647–55.
36. S. Yamaguchi, H. Makino, A. Sakatoku, and Y. Iguchi: *3rd Int. Conf. on Zinc and Zinc Alloy Coated Steel Sheet: Galvatech '95 Conf. Proc.*, Chicago, IL, 1995, Iron and Steel Society, Warrendale, PA, 1995, pp. 787–94.
37. J.R. McDermid and W.T. Thompson: *44th Mechanical Working and Steel Processing Conf. Proc.*, Orlando, FL, 2002, Iron and Steel Society, Warrendale, PA, 2002, pp. 805–13.
38. J.R. McDermid, E. Baril, and W.T. Thompson: *6th Int. Conf. on Zinc and Zinc Alloy Coated Steel Sheet: Galvatech '04 Conf. Proc.*, Chicago, IL, 2004, Association for Iron and Steel Technology, 2004, pp. 491–99.
39. M.H. Kaye, W.T. Thompson, and J.R. McDermid: *Materials Science and Technology 2005 Conf. Proc.–Developments in Sheet Products for Automotive Applications*, Association for Iron and Steel Technology, Pittsburgh, PA, 2005, pp 199–210.
40. V. Rajhavan: *J. Phase Equil.*, 2003, vol. 24 (6), pp. 546–50.
41. ASTM B6–03, *Annual Book of ASTM Standards: 2004*, ASTM International, West Conshohocken, PA, 2004, vol. 02.04, pp. 1–3.
42. M. Gagné, H. Guttman, J. L'Ecuyer, G.G. Brummitt, G.L. Adams, and D. Kleimeyer: *Proc. 82nd Galvanizer's Association Meeting*, Niagara Falls, NY, Galvanizer's Association, 1990, pp. 125–45.
43. F. Kohler: *Monatsh. Chem.*, 1960, vol. 91, pp. 738–40.
44. A.D. Pelton and W.T. Thompson: *Prog. Solid State Chem.*, 1975, vol. 10 (3), pp. 119–55.
45. M.H. Kaye, K.M. Jaansalu, and W.T. Thompson: in *Measurement of the Thermodynamic Properties of Multiple Phases*, R.D. Weir and T.W. de Loos, eds., IUPAC, Elsevier, Amsterdam, Netherlands, 2005, pp. 275–305.
46. M.H. Kaye, K.M. Jaansalu, and W.T. Thompson: *Can. Metall. Q.*, 2003, vol. 42 (4), pp. 393–410.
47. J.L. Murray: *Bull. Alloy Phase Diag.*, 1983, vol. 4 (1), pp. 55–73.
48. B.P. Burton and P. Perrot: *Phase Diagrams of Binary Iron Alloys*, ASM, Metals Park, OH, 1993, pp. 459–66.
49. U.R. Kattner and B.P. Burton: *Phase Diagrams of Binary Iron Alloys*, ASM, Metals Park, OH, 1993, pp. 12–28.
50. C.W. Bale and A.D. Pelton: *Metall. Trans. A*, 1990, vol. 21A, pp. 1997–2002.
51. S. an Mey: *Z. Metallkd.*, 1993, vol. 84 (7), pp. 451–55.
52. X. Su, N.-Y. Tang, and J.M. Toguri: *J. Alloys Compd.*, 2001, vol. 325, pp. 129–36.
53. G. Reumont, P. Perrot, J.M. Fiorani, and J. Hertz: *J. Phase Equil.*, 2000, vol. 21 (4), pp. 371–78.
54. J. Nakano, D.V. Malakhov, and G.R. Purdy: *Comput. Coupl. Phase Diag. Thermochem.*, 2005, vol. 29, pp. 276–88.
55. O. Kubaschewski: *Iron Binary Phase Diagrams*, Springer-Verlag, New York, NY, 1982, pp. 86–87.
56. ASTM B852–01, *Annual Book of ASTM Standards: 2004*, ASTM International, West Conshohocken, PA, 2004, vol. 02.04, pp. 1024–26.